

RESEARCH ARTICLE

Formation and maintenance of subsiding shells around non-precipitating and precipitating cumulus clouds

Julien Savre 

Meteorological Institute, Physics
Department, Ludwig-Maximilians-
Universität München, Munich, Germany

Correspondence

Julien Savre,
Ludwig-Maximilians-Universität,
Theresienstrasse 37, 80333 München,
Germany.
Email: Julien.Savre@lmu.de

Abstract

A shell of subsiding air is generally known to develop around cumulus clouds and shield them from their environment. We seek here to improve our understanding of such shells by (a) revealing the detailed vertical and horizontal structure of shells surrounding both shallow and deeper clouds, and (b) identifying the mechanisms responsible for in-shell subsidence generation and maintenance. To that end, a high-resolution Cloud Resolving Model simulation of the shallow-to-deep convection transition over a tropical land surface is analysed with an emphasis on the cloud's near environment. Shells surrounding shallow and deep clouds are found to possess surprisingly similar characteristics. However important differences are observed near cloud top where the deepest clouds are associated with stronger subsidence and broader shells. In the convective outflow region, stronger in-shell subsidence coincides with strong buoyancy reversal, but also with strong pressure gradients naturally generated by cloud-top vortex dynamics. A more delicate balance between various processes takes place below, and in-shell subsidence is only barely sustained as buoyancy reversal is largely compensated by pressure gradients. Finally, while evaporation is clearly the main source of buoyancy reversal everywhere around cloud edges, it is also shown that the downward transport of warmer air from aloft through the subsiding shells may compensate for evaporative cooling to slowly bring in-shell buoyancy to a near-neutral state. Overall, while it cannot be denied that evaporative cooling and buoyancy reversal play important roles in generating and sustaining in-shell subsidence, the present results also emphasise that mechanical forcing at cloud top and downward transport within the shells should not be overlooked.

KEYWORDS

cloud dynamics, near-cloud environment, subsiding shells, tropical convection.

1 | INTRODUCTION

Entrainment and detrainment in cumulus clouds are generally understood as the processes through which a cloud exchanges mass, energy and momentum with its environment (de Rooy *et al.*, 2012). They exert a strong control on the fate of cumulus clouds, and constitute key elements of any mass-flux-based convective parametrization used in numerical weather prediction systems and climate models. As such, they also constitute an important source of model uncertainties as they remain largely unconstrained (Rougier *et al.*, 2009).

To this day, no existing parametrization for entrainment–detrainment rates has given full satisfaction. The current lack of an adequate parametrization can be explained by various complicating factors. For example, entrainment and detrainment result from the combined effects of different physical mechanisms which are sometimes difficult to disentangle (adiabatic expansion, turbulent mixing, microphysics, etc.) These difficulties are somehow accentuated by the fact that a parcel's momentum and thermodynamic properties may not be diluted at the same rates since they are not subject to the same constraints (Sherwood *et al.*, 2013). In addition, these mixing rates generally show poor correlations with the clouds macro- and micro-physical properties such that no physically sound and systematically reliable relationship has yet been found (Lu *et al.*, 2016). Finally, there exists evidence that entrainment and detrainment are stochastic processes which can therefore not be correctly captured by deterministic approaches (Romps and Kuang, 2010).

Another factor influencing entrainment and detrainment in cumulus clouds is the existence of a relatively cold and moist shell of subsiding air surrounding them, and shielding them from the warmer and drier environment (Jonas, 1990; Rodts *et al.*, 2003; Heus and Jonker, 2008; Dawe and Austin, 2011; Zhang *et al.*, 2016). Moist convection parametrizations indeed generally assume that clouds are mixed directly with their far-field environment having properties of the averaged atmosphere at this level. This assumption constitutes the basis of many entraining plume models used to characterise the structure of cumulus clouds in typical mass flux schemes (Tiedtke, 1989; Soares *et al.*, 2004), and ignores the existence of moist subsiding shells. However, as shown by Dawe and Austin (2011), this approximation has the potential to introduce important biases when calculating convective cloud properties, and may explain most of the discrepancies observed when comparing bulk and direct entrainment rate estimates (Romps, 2010; Dawe and Austin, 2011). Unfortunately, as long as the characteristics and dynamics of subsiding shells, as well as their exact role played in the entrainment–detrainment process are not

elucidated, it is unlikely that cloud shells can be adequately incorporated in plume models. So far, only few authors have proposed simple ways to explicitly account for subsiding shells in these models (Heus and Jonker, 2008; Hannah, 2017).

Subsiding shells are thought to stem from the evaporation of cloud particles around cloud edges where mixing with the dry environment occurs. Evaporation then locally cools the air to the point where it can become negatively buoyant and sink (Heus and Jonker, 2008; Wang *et al.*, 2009; Katzwinkel *et al.*, 2014; Park *et al.*, 2016). This explanation is in line with the buoyancy sorting concept from Blyth *et al.* (1988) often used as a simple paradigm to understand and parametrize lateral entrainment and detrainment in cumulus clouds. However, although the existence of such shells has now been extensively proven and analysed from aircraft measurements (Jonas, 1990; Rodts *et al.*, 2003; Blyth *et al.*, 2005; Damiani *et al.*, 2006; Wang *et al.*, 2009; Wang and Geerts, 2010; Katzwinkel *et al.*, 2014; Schmeissner *et al.*, 2015; Mallaun *et al.*, 2019) and numerical simulations (Heus and Jonker, 2008; Jonker *et al.*, 2008; Heus *et al.*, 2009; Dawe and Austin, 2011; Abma *et al.*, 2013; Glenn and Krueger, 2014; Park *et al.*, 2016; 2017; Nair *et al.*, 2019), the exact mechanisms responsible for their formation and maintenance remain unclear, and are still debated. For example, Park *et al.* (2016), (2017) have recently formulated the hypothesis that buoyancy reversal inside subsiding shells actually originates from the detrainment of denser air transported upwards by convective updraughts, and is only incidentally affected by evaporative cooling.

This work uses high-resolution numerical simulations to elucidate key questions regarding the origin and dynamics of subsiding shells developing around shallow non-precipitating, and deeper precipitating (*cumulus congestus*) clouds. In particular, the main outcomes of this study can be summarised as follows:

1. Whereas most previous works have focused on either shallow cumuli (Heus and Jonker, 2008; Jonker *et al.*, 2008; Dawe and Austin, 2011; Park *et al.*, 2016) or convective cloud ensembles including clouds of various sizes (Glenn and Krueger, 2014), the similarities and differences between shells developing around shallow and deeper clouds are here emphasised by dividing the simulated cloud population according to their depth.
2. The complete two-dimensional structure of subsiding shells is characterized using a compositing method similar to Wang *et al.* (2009), where existing studies have essentially focused only on horizontal cuts through clouds (Heus and Jonker, 2008; Jonker *et al.*, 2008), or shell structures in conserved variable space (Glenn and Krueger, 2014; Park *et al.*, 2017).

3. Two-dimensional composites are also used to propose a comprehensive budget analysis for both vertical momentum and virtual potential temperature to help understand the mechanisms leading to the formation and maintenance of these shells.

In practice, a Cloud-Resolving Model (CRM; Savre *et al.* (2014)) is used to simulate the transition from shallow to deep convection (up to about 8 km deep) over the tropical continent in a very idealized set-up (Grabowski *et al.*, 2006). The model operates at a horizontal resolution of 25 m. This is thought to be small enough to resolve the dynamics responsible for small-scale mixing at the cloud interface (Craig and Dörnbrack, 2008), and absolutely necessary to capture the structure of the narrowest subsiding shells which are generally found to be at most 100 to 200 m wide (Wang *et al.*, 2009; Katzwinkel *et al.*, 2014).

In the following, Section 2 describes the methods used, including the numerical set-up and compositing method. In Section 3, basic cloud shell statistics are presented showing for instance how the mean shell width and strength vary as a function of cloud type and altitude. Results from the compositing approach are then discussed in Section 4, where the two-dimensional structure of subsiding shells, as well as the mechanisms responsible for their formation and maintenance are investigated. Finally, conclusions are drawn in Section 5.

2 | SIMULATION AND METHODS

2.1 | The model

The results presented hereafter were obtained using the MISU-MIT Cloud and Aerosol model (MIMICA; Savre *et al.*, 2014). MIMICA solves governing equations for the three momentum components $\rho_0 u$, $\rho_0 v$ and $\rho_0 w$ (ρ_0 being the horizontally homogeneous reference density), potential temperature θ , total water mass mixing ratio q_t , as well as relevant cloud microphysical quantities. The current version of the model employs the anelastic formulation from Lipps and Hemler (1982) to efficiently filter out sound waves, and solves all equations in conservative form on a staggered Arakawa C-grid. Scalar quantities are advected using a Total-Variation Diminishing (TVD), flux-limited version of the Lax–Wendroff scheme, while momentum advection is performed using a centred fourth-order finite difference scheme. Time integration is performed using a low-storage third-order Runge–Kutta scheme.

Cloud microphysics are parametrized following Grabowski (1998). The only conserved variables are the mass mixing ratios of non-precipitating and precipitating

condensed water particles, q_l and q_p respectively. The partitioning between liquid and cloud ice then depends linearly on temperature between 273.15 K (all liquid) and 253.15 K (all ice). Precipitating particles are distributed according to the Marshall–Palmer size distribution with a fixed pre-exponential factor $N_0 = 10^7 \text{ m}^{-4}$. All microphysical processes including rain autoconversion, accretion, deposition–evaporation and sedimentation, are parametrized according to Grabowski (1998). Saturation adjustment is employed to model the growth of non-precipitating particles.

Turbulent mixing is represented using a 1.5-order scheme with prognostic turbulent kinetic energy (Moeng, 1984). Exchanges of heat and moisture at the surface are simply treated using fixed fluxes, while momentum fluxes are ignored. Note that no parametrized radiation was employed in the model (Section 2.2).

2.2 | Numerical set-up

The numerical experiment is based on the Large-scale Biosphere–Atmosphere (LBA) model intercomparison study from Grabowski *et al.* (2006), with further idealizations from Wu *et al.* (2009) and Böing *et al.* (2012). The initial temperature profile is taken from Grabowski *et al.* (2006), while relative humidity is held constant and equal to 85% between the surface and 2,500 m, equal to 80% between 2,500 and 6,000 m, and decreases linearly above to 15% at 18,000 m. These conditions are somewhat similar to the M80 experiment in Wu *et al.* (2009) except for the slower decrease of RH above 6,000 m. Horizontal winds are initially set to $0 \text{ m}\cdot\text{s}^{-1}$ everywhere. Convection is initiated by prescribing potential temperature perturbations uniformly distributed between -0.1 and $+0.1$ K below 200 m. Following Böing *et al.* (2012), surface sensible and latent heat fluxes are set to 161 and $343 \text{ W}\cdot\text{m}^{-2}$ respectively, and are held constant throughout the simulation. In the absence of interactive radiation, the clouds develop under constant forcing, without a true diurnal cycle.

The numerical domain is doubly periodic in the horizontal plane, and is discretised using $2,048 \times 2,048$ grid points with a grid spacing $\Delta x = \Delta y = 25 \text{ m}$. Sensitivity experiments performed varying the model's horizontal resolution from 100 to 25 m (not shown) suggested that such a high horizontal resolution is necessary to adequately capture the structure of the narrow mixing layer developing between the clouds and their environment. The domain extends vertically up to 14,200 m and uses a stretched grid of 160 points, with a vertical resolution of $\Delta z = 30 \text{ m}$ below 2,000 m, geometrically unrefined above. A Rayleigh damping layer is used above 12,000 m with a relaxation

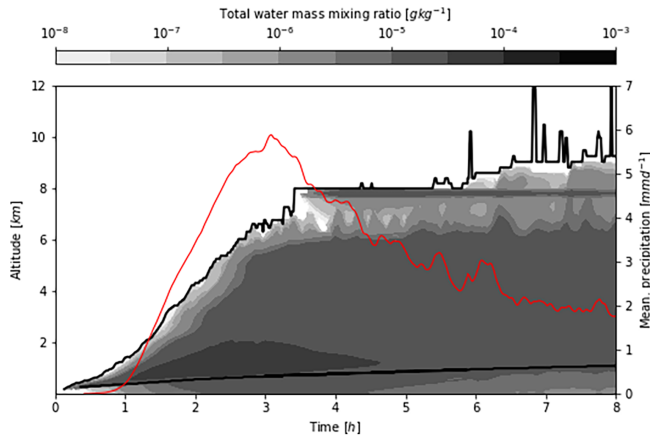


FIGURE 1 Time series of horizontally averaged condensed water mass mixing ratio. The upper and lower solid black lines represent the position of maximum cloud top and mean cloud base respectively. The thin solid red line represents the mean surface precipitation in the domain (right axis)

time-scale of 2 hr. Horizontal winds are nudged back to their initial values with a time-scale of 6 hr.

2.3 | Data analysis

The first shallow, non-precipitating clouds form quickly after the initialization time t_0 , and precipitation reaches the surface very shortly after, within the first hour (Figure 1). Three hours later, at $t_0 + 3.5$ hr, clouds reach their maximum altitude at about 8 km. Data are then extracted and analysed between $t_0 + 4$ hr and $t_0 + 8$ hr, a period over which the simulated cloud field seems to have reached a quasi-stationary state despite the mean precipitation rate across the domain decreasing continuously. After 6 hr, the maximum cloud-top height exhibits strong oscillations between 8 and 12 km due to the presence of high-altitude clouds and cloud remnants which will be excluded later from the analysis. The evolution of the cloud field depicted on Figure 1 is consistent with results obtained by Wu *et al.* (2009) and Böing *et al.* (2012) using similarly idealized set-ups. In particular, we see a progressive deepening of the cloud layer starting during the first hour of simulation, until surface precipitation reaches a maximum, with the deepest clouds then attaining altitudes >8 km.

The main results of this work are obtained by compositing convective clouds in a way similar to Wang *et al.* (2009). Cloud objects are first identified from two-dimensional slices extracted from the full three-dimensional simulation. At each analysis time, 15 slices are extracted in both X and Y directions, using a constant spacing between slices of 3,200 m to limit the risk of sampling the same

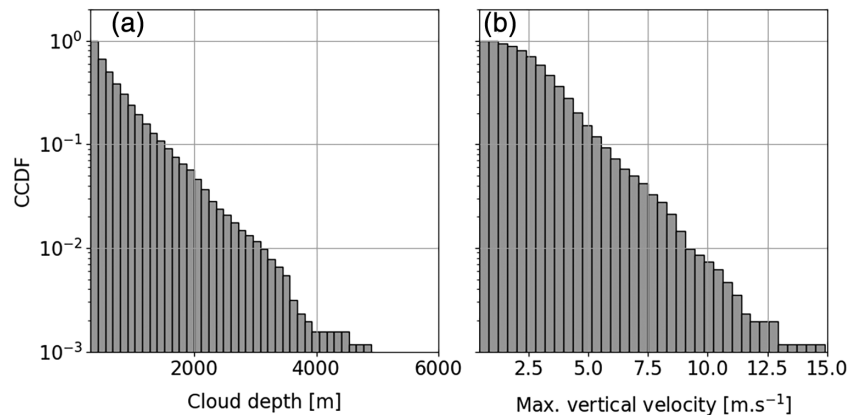
clouds twice. The procedure is then repeated every 30 min between times $t_0 + 4$ hr and $t_0 + 8$ hr, yielding a total of 270 two-dimensional slices to be analysed.

Cloud objects are defined as clusters of contiguous grid cells (in both the horizontal and vertical directions) with condensed water content $q_1 + q_p$ exceeding $0.01 \text{ g}\cdot\text{kg}^{-1}$ and updraught velocity w larger than $0 \text{ m}\cdot\text{s}^{-1}$. The subcloud region is excluded from each cloud object by considering only points situated above cloud base. This latter is defined locally as the first vertical level where the non-precipitating water content q_1 exceeds $0.01 \text{ g}\cdot\text{kg}^{-1}$. Similar cloud definitions based on a combination of both condensed water and vertical velocity thresholds were used in previous studies on subsiding shells (Heus and Jonker, 2008; Glenn and Krueger, 2014). By extension, cloud shells are defined as all grid points within a certain distance from the nearest cloud object with either $q_1 + q_p < 0.01 \text{ g}\cdot\text{kg}^{-1}$, or $w < 0 \text{ m}\cdot\text{s}^{-1}$.

When compositing convective clouds, only condensed water clusters with bases between 1,000 and 2,000 m are considered to exclude mid-tropospheric convection and high-altitude cloud remnants from the analysis. In addition, each cluster must be at least 300 m thick (at these altitudes, with a vertical resolution of 30 m, the smallest clouds in the analysis contain at least 10 grid points, which was found to be sufficient to guarantee the quality of the results), and at least 2,500 m away from the nearest cloud to limit direct shell-shell or cloud-shell interactions (as shown later, most shells are at most 2,500 m wide). After this first selection, 2,563 clouds remain to be analysed, corresponding to an average of ~ 9.5 cloud objects per slice. We further split the remaining cloud population into three main categories based on their statistical properties (see the complementary cumulative distributions plotted in Figure 2): ‘shallow clouds’ are defined as all clouds belonging to the 60th percentile of cloud depth, equivalent to a maximum depth of 690 m; ‘deep clouds’ are clouds larger than the 90th percentile of cloud depth, equivalent to a minimum depth of 1,500 m; and ‘active clouds’ constitute the 25% most active deep clouds, corresponding to a maximum core updraught velocity w_{max} larger than $8 \text{ m}\cdot\text{s}^{-1}$. Results presented below were found to depend only weakly on these thresholds. Using this partitioning technique, 1,576 shallow clouds, 257 deep clouds and 67 active clouds were identified. It should be remembered here that the aforementioned categories remain purely empirical since there does not exist a clear and objective way to separate shallow and deep clouds.

Once individual clouds are identified in the two-dimensional slices, compositing is performed by first associating each grid cell in individual slices (including cloudy grid cells) with its nearest cloud object. Then, the horizontal distance between the considered grid point

FIGURE 2 Complementary cumulative distribution functions (CCDFs) of (a) cloud depth, and (b) maximum vertical velocity in clouds, for all clouds analysed



and the edge of the nearest cloud is computed, setting the location of the edge as the reference. We can then average any local property of the simulated field conditioned on both altitude z and the nearest cloud edge distance. We can further define a normalised vertical coordinate within each cloud as $z^* = (z - z_{\text{base}})/(z_{\text{top}} - z_{\text{base}})$, with z_{top} and z_{base} denoting cloud-top and cloud-base altitudes respectively. By doing so, it becomes possible to analyse the two-dimensional structure of cloud cores and their near environment independently of cloud depth.

3 | MEAN SHELL PROPERTIES

3.1 | Shell characteristics

In this section, bulk shell properties calculated for all shallow, deep and active clouds are analysed. Cloud shells are here defined as all non-cloudy grid points satisfying $w < 0 \text{ m}\cdot\text{s}^{-1}$ and continuously connected to the nearest cloud at a given altitude. In practice, cloud shells are identified as follows (also Figure 3):

1. At any given altitude, the position of the edges of each individual cloud object is recorded;
2. Moving away from each edge into the environment one grid point at a time, the considered point is assumed to belong to the shell if its velocity $w < 0 \text{ m}\cdot\text{s}^{-1}$;
3. If this condition is met, the properties of the current shell (minimum velocity, width, thermodynamic structure...) are updated based on local grid point values, and step 2 is repeated moving one grid cell further away from the edge;
4. If $w > 0 \text{ m}\cdot\text{s}^{-1}$, the search is stopped and the shell's properties at that altitude are stored.

After all shells of all cloud objects identified at any given level have thus been constructed, shell statistics can easily be computed and analysed.

Figure 4 displays vertical profiles of averaged in-shell minimum vertical velocity w_{min} (Figure 4a, e), and minimum buoyancy b_{min} (Figure 4b, f) as functions of both altitude and normalised height in clouds. Buoyancy is here defined as $b = \rho_0 g(\theta_v/\theta_{v0} - 1)$, with g the gravitational acceleration, $\theta_v = \theta[1 + \epsilon q_t - (1 + \epsilon)q_c]$ the virtual potential temperature, θ_{v0} its background reference value, q_t the total water mixing ratio, q_c the condensed water mixing ratio, θ the potential temperature and $\epsilon \approx 0.602$.

Below 2000 m, given a certain environment, there do not appear to be significant differences between subsiding velocities for shells surrounding shallow and deep clouds (on average $\sim -1.2 \text{ m}\cdot\text{s}^{-1}$ independently of altitude; Figure 4a). In contrast, subsiding shells surrounding deep clouds strengthen when moving higher in altitude (up to $-2 \text{ m}\cdot\text{s}^{-1}$ on average for active deep clouds, with an absolute maximum of $-4 \text{ m}\cdot\text{s}^{-1}$ at 5,000 m). This difference is perhaps a result of the drier environment found near the tops of the deeper clouds and favouring evaporative cooling, but it may as well be related to the stronger dynamics of vortical structures found at the top of the deepest thermals. Figure 4b and f reveal that the in-shell minimum buoyancy, b_{min} , remains relatively constant with altitude and does not differ much between deep and shallow cloud shells (remaining on average close to $-10 \text{ g}\cdot\text{m}^{-2}\cdot\text{s}^{-2}$). Interestingly, a b_{min} maximum is found near the top of the deepest clouds where w_{min} reaches a minimum, which may appear as counterintuitive.

Shell width statistics are also plotted on Figure 4. The negatively buoyant part of all subsiding shells is here identified separately and referred to as the ‘inner shell’ region (a similar distinction was made by e.g., Katzwinkel *et al.*, 2014). In short, subsiding shell points must in addition satisfy the condition $b < 0 \text{ kg}\cdot\text{m}^{-2}\cdot\text{s}^{-2}$ to also belong to the inner shell (Figure 3). The respective widths of the subsiding and inner shells are then calculated as the distances between the nearest cloud edge and the first point into the environment where either $w \geq 0 \text{ m}\cdot\text{s}^{-1}$ (subsiding shell) or $b \geq 0 \text{ kg}\cdot\text{m}^{-2}\cdot\text{s}^{-2}$ (inner shell). Both shallow and

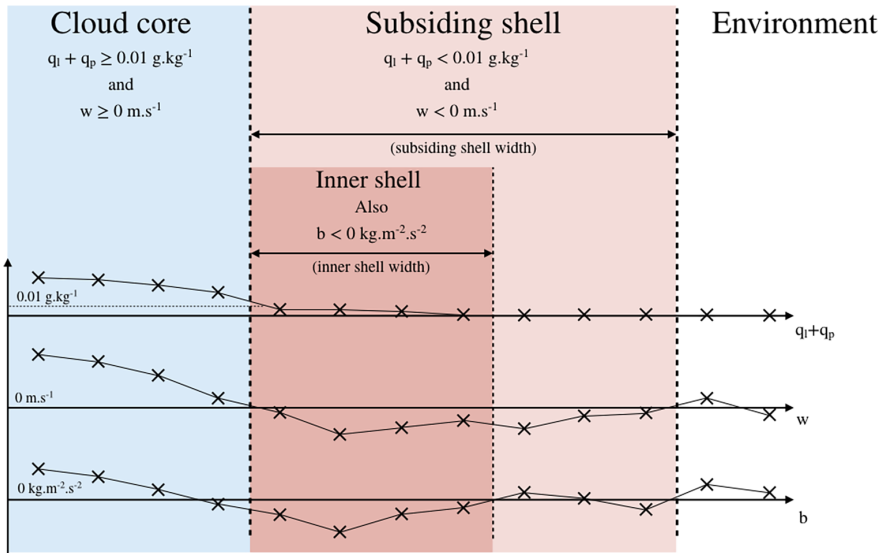


FIGURE 3 Conceptual representation of how clouds and their shells are defined in this work. Subsiding shells correspond to the continuous region directly surrounding clouds with $w < 0 \text{ m.s}^{-1}$. The inner shell region is defined as the part of the subsiding shell directly adjacent to the cloud, satisfying, in addition, $b < 0 \text{ kg.m}^{-2}.\text{s}^{-2}$

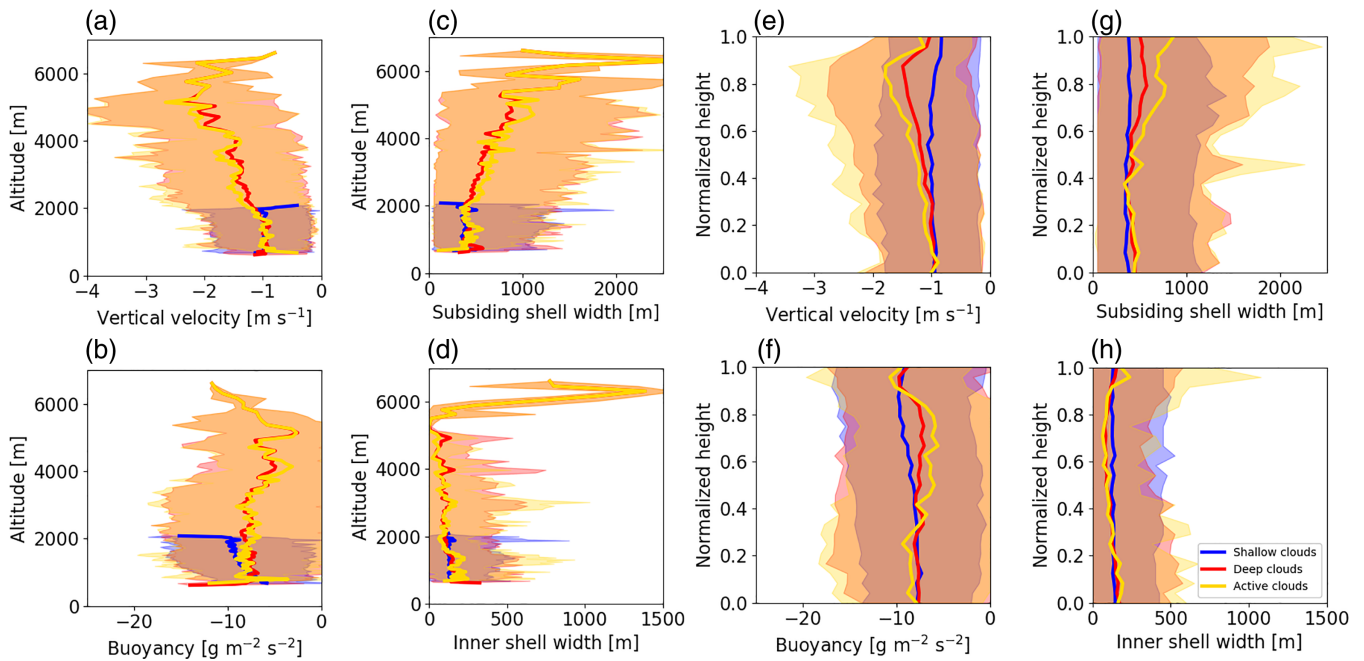


FIGURE 4 (a, e) Minimum downdraught velocity, (b, f) minimum negative buoyancy, (c, g) downdraught shell width, and (d, h) buoyancy shell width calculated for all shallow, deep and active clouds. (a–d) show variables as a function of altitude above ground, and (e–h) as a function of normalised height in clouds. Solid lines represent averages over all clouds identified in a given category. Colour shadings indicate the 5th to 95th percentile region for the three categories

deep cloud shells are very similar in strength and width near their base. However, near their top, deep cloud shells are clearly wider ($\sim 800 \text{ m}$ on average, with a maximum of $\sim 2,000 \text{ m}$) than shallower clouds ($\sim 400 \text{ m}$ on average, with a maximum of $\sim 1,400 \text{ m}$). Surprisingly, the mean inner shell width appears to be mostly independent of both cloud type and altitude. This is particularly apparent on Figure 4h in normalised cloud height coordinates. Inner shells remain generally narrower than 500 m , and are on

average about 150 m wide. They occupy about a third to a half of the entire subsiding shells. Given that the model was operated at 25 m resolution, inner shells contain on average six grid points which can be regarded as sufficient to capture their detailed structure.

Distributions of minimum in-shell vertical velocity, buoyancy and shell width are plotted on Figure 5 at three different altitudes for all clouds. The w_{\min} and b_{\min} PDFs exhibit clear peaks that move towards larger

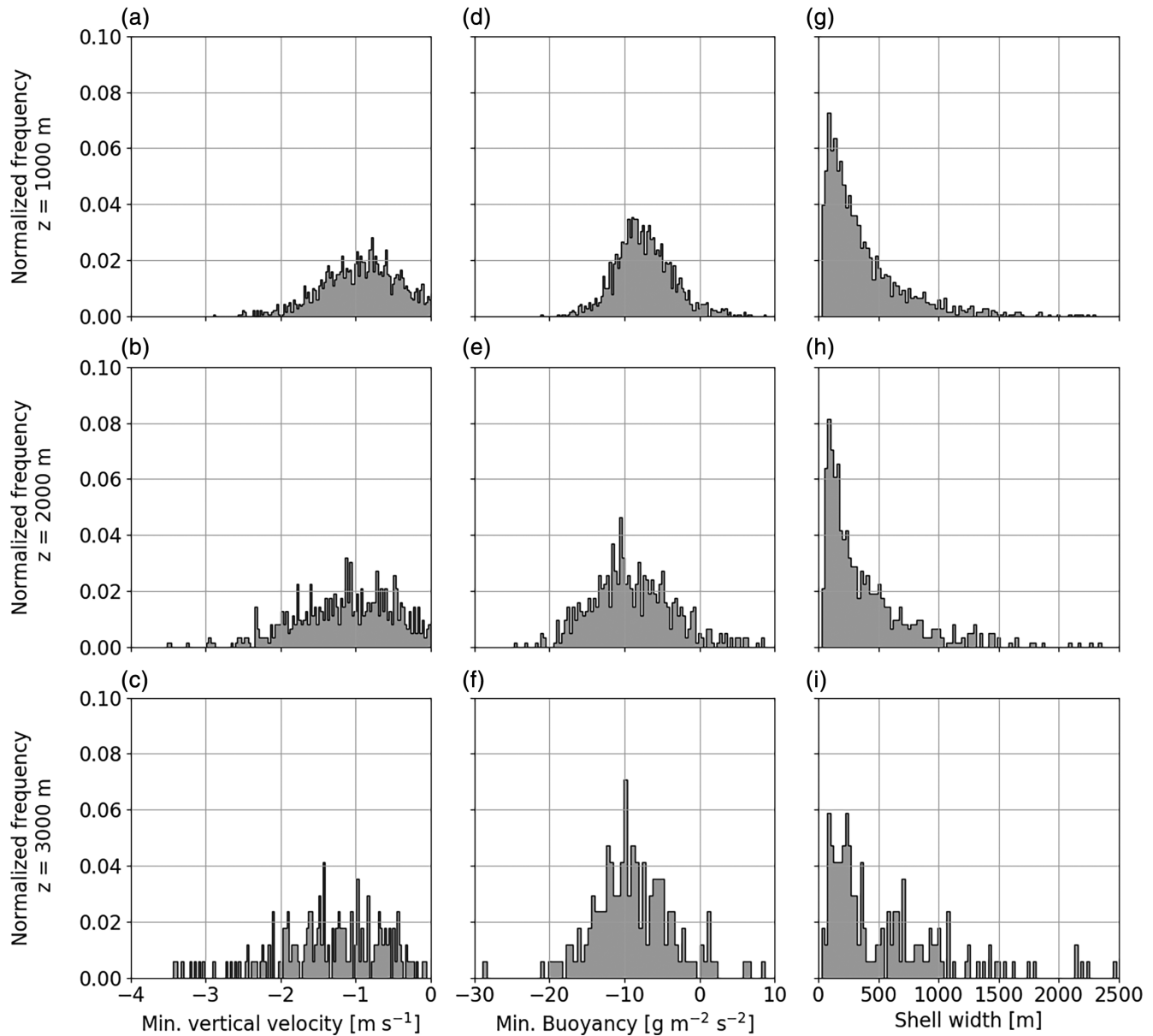


FIGURE 5 PDFs of all (a–c) in-shell minimum vertical velocity, (d–f) in-shell minimum buoyancy, and (g–i) total shell width at altitudes (a, d, g) 1000 m, (b, e, h) 2000 m and (c, f, i) 3000 m. No distinction is made here between shallow, deep and active clouds

absolute values as altitude increases (from $-0.8 \text{ m}\cdot\text{s}^{-1}$ at 1,000 m to $-1.5 \text{ m}\cdot\text{s}^{-1}$ at 3,000 m for w_{\min} , and from -8 to $-10 \text{ g}\cdot\text{m}^{-2}\cdot\text{s}^{-2}$ for b_{\min}). In addition, the spread of both PDFs tends to increase with altitude. Neutral and negatively buoyant shells exist and represent from 4.5% at 1,000 m to almost 9% at 3,000 m of the whole shell population. Looking at shell width distributions, a clear peak at 100 m is consistently seen at all altitudes. This supports the idea that the 25 m horizontal resolution adopted is able to resolve the structure of most subsiding shells sampled. Note however that the probability of finding very narrow shells occupying one or two grid points remains always large, although this may be biased by the $0 \text{ m}\cdot\text{s}^{-1}$ velocity threshold used, which makes the identification of

individual shells sensitive to turbulence intermittency in the near-cloud environment.

Figure 6a displays the correlation between maximum cloud core and minimum in-shell vertical velocities. Clearly, in-shell subsidence strength increases linearly as the corresponding cloud cores accelerate. Further, the altitude at which in-shell maximum subsidence is recorded generally corresponds to the altitude at which the maximum updraught velocity is reached inside the cloud (Figure 6b). Actively growing clouds characterised by stronger updraught cores are therefore also associated with stronger subsidence along their edges. Besides, the correlation between the altitudes at which the maximum shell width and maximum cloud core velocity are recorded

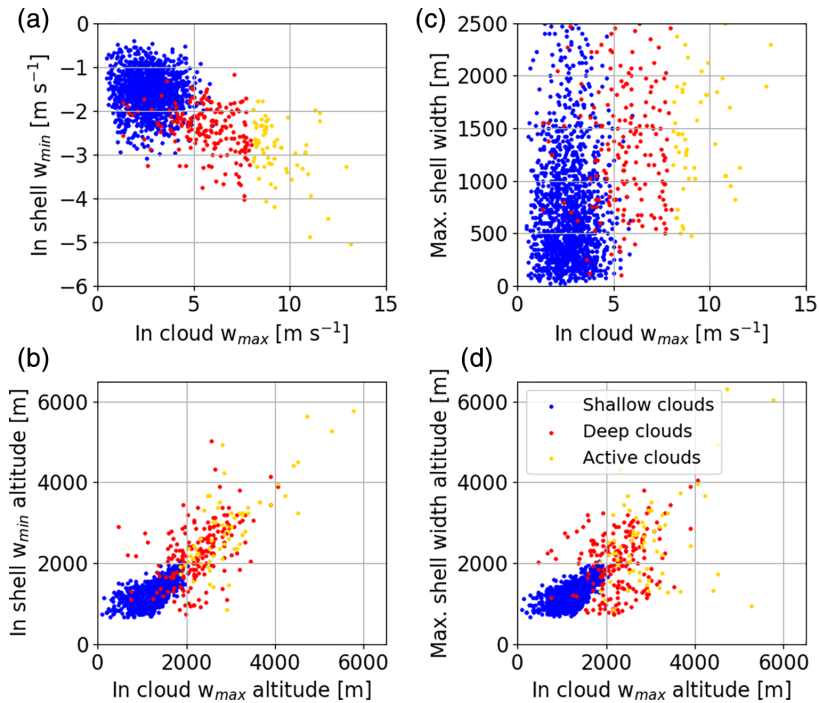


FIGURE 6 Scatter plots of (a) in-shell minimum vertical velocity and (c) maximum shell width as functions of maximum cloud core updraught velocity. The altitudes at which (b) the shell minimum velocity and (d) the maximum width were attained are displayed as functions of the altitudes at which cloud cores reach their maximum updraught velocity. Each individual marker represents a single cloud and its shell

is also relatively good, despite the fact that the quantities correlate very poorly (Figure 6c, d). More generally, cloud shells tend to be more strongly subsiding and wider at the level where cloud cores reach their maximum updraught velocity.

3.2 | In-shell thermodynamics

Vertical profiles of in-shell and in-cloud potential temperature θ , water vapour mixing ratio q_v and moist static energy MSE anomalies are plotted on Figure 7. Anomalies are here calculated by subtracting from local quantities their horizontal averages taken across all environmental grid points (that is non-cloudy points, which includes cloud shells). MSE is defined as $MSE = c_p T + L_v q_v + gz$, with c_p the heat capacity of dry air at constant pressure, L_v the latent heat of vaporisation, g the gravitational acceleration, T the temperature, q_v the water vapour mixing ratio and z the altitude.

Subsiding shells are overall moister and colder than the environment, independently of cloud type and altitude. As expected, in-cloud MSE anomalies are positive throughout the cloud layer, indicating that cloudy air at a given altitude generally originates from lower levels. In-shell MSE anomalies follow the same trends as q_v anomalies, remaining mostly positive and slowly decreasing from $\sim 1 \text{ kJ}\cdot\text{kg}^{-1}$ at cloud base to almost 0 at 4,000 m and above. That in-shell q_v and MSE lie exactly between the cloudy and environmental values at a given level can be interpreted as a manifestation of lateral mixing between

the clouds and their environment. Since in-shell MSE anomalies decrease with altitude, one may speculate that subsiding shells contain on average a larger fraction of cloud air near their base than near their top. However the reasons for this behaviour are not clear. While in-shell θ anomalies are always negative independently of cloud type and altitude, they remain mostly negative inside shallow clouds, but positive inside deep clouds, except near their base. In this situation, a cloudy air parcel that is colder than its environment and detrained from the cloud will contribute to buoyancy reversal in the near-cloud environment even in the absence of evaporative cooling.

Figure 8 displays the shell structure in $MSE-z$ coordinates, similar to Glenn and Krueger (2014). Individual grid points have been sampled in all cloud shells, defined as previously as all points directly connected to a cloud object with $w < 0 \text{ m}\cdot\text{s}^{-1}$ (also Figure 3). The mean environment, cloud and shell air profiles are also plotted. As already seen in Figure 7, cloudy air has a higher MSE than environmental air at all levels. In addition, below $\sim 4,000 \text{ m}$, the mean shell profiles generally lie exactly between the environment and cloud profiles, with mean in-shell MSE values remaining always close to the environmental ones. Above that level, the shell profiles follow more closely the environment ones, suggesting that shell air is here composed almost exclusively of environmental air. This may be connected to the fact that subsiding shells are generally broader in this region.

Negatively buoyant parcels are generally found exactly between the mean cloud and mean environment profiles. Moving away from this region, a large fraction of

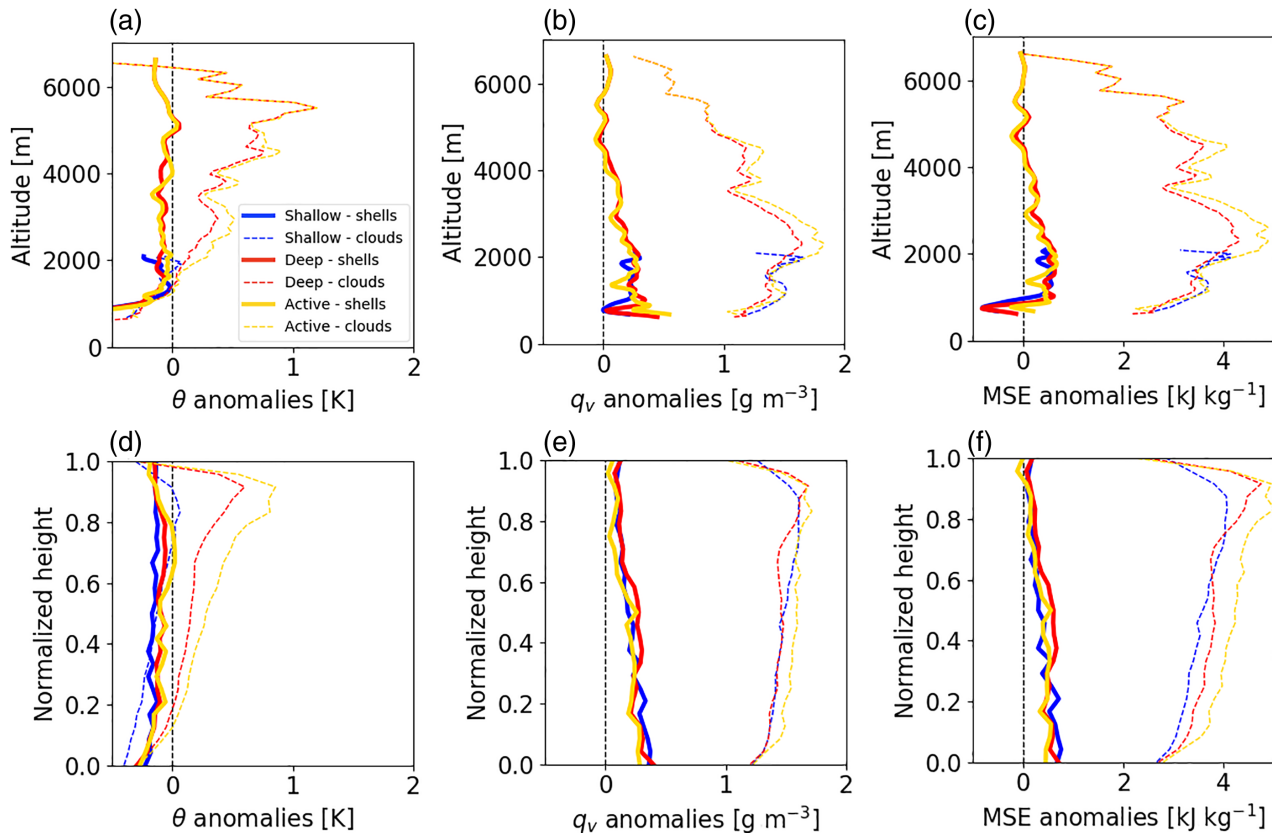


FIGURE 7 Mean in-shell (a, d) potential temperature θ , (b, e) water vapour mass concentration q_v and (c, f) moist static energy anomalies calculated with respect to environmental values for all shallow, deep and active clouds, as a function of (a–c) altitude above ground, and (d–f) normalised height in clouds

all sampled subsiding points remain positively buoyant. When located near the mean cloud profiles, buoyant air parcels are composed of cloudy air that has not been diluted enough by the environment for buoyancy reversal to happen. When located near the mean environmental profiles, the buoyant parcels may be composed of low-*MSE* air from upper levels transported downward within the subsiding shells. However it is difficult to ascertain this hypothesis based on a mixing diagram analysis only. Overall, the mean shell profiles generally lie in a region of almost neutrally buoyant air.

4 | CLOUD AND SHELL COMPOSITES

4.1 | General description

Cloud and shell composite structures are shown on Figure 9 in normalised cloud height coordinates z^* . Figure 9a, d show vertical velocity composites, b, e buoyancy composites, and c, f horizontal divergence composites. In all plots, the zero position on the horizontal axis, denoted by vertical dashed lines, indicates the

position of the cloud edges. Note that, since deep cloud composites were found to be dominated by active clouds, composites for the latter are not shown.

Looking at vertical velocity composites, a striking difference between shallow and deep clouds emerges, with shallow clouds characterised by a weaker and relatively homogeneous core updraught, while deep clouds are clearly driven by large vortex-like structures near their top. Buoyancy inside the clouds reaches a maximum in a shallow layer near cloud top, slightly above the updraught velocity maximum. In addition, a buoyancy minimum is consistently seen near cloud base, reflecting the existence of convective inhibition between cloud base and $\sim 1,000$ m.

Subsiding shells are clearly visible on Figure 9a, d where coherent downdraughts approximately 500 m wide extend throughout the depth of both shallow and deep clouds. The structure of these shells correlates well with that of the inner part of the clouds: a clear velocity minimum is reached at the exact same altitude where the updraught velocity reaches its maximum within the cloud core. Besides, buoyancy reversal is consistently stronger near the top of all clouds. Again, this buoyancy extremum is located slightly above the in-shell velocity minimum. Below, buoyancy remains negative over a narrow band

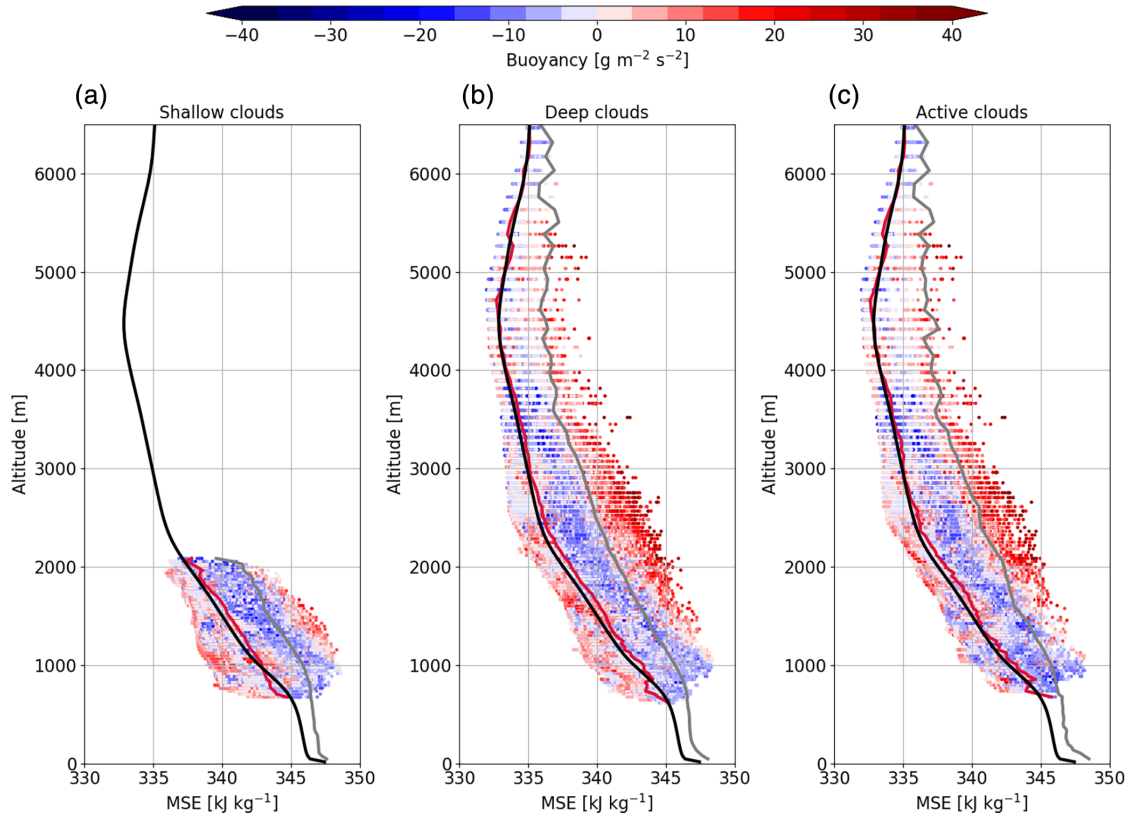


FIGURE 8 Scatter plots of in-shell buoyancy (colour) in MSE –altitude coordinates. Each single point was taken inside shell regions (the text gives definitions of the shell in this context) surrounding (a) shallow, (b) deep and (c) active clouds. Mean environmental (black), cloud (grey) and shell (red) profiles are also displayed

around all clouds (the ‘inner shell’), with no clear difference in strength or width between shallow and deep clouds. Horizontal divergence in a shallow layer at the top of all clouds can be seen on Figure 9c, f, with comparatively weak convergence in the environment at the same levels. This marks the main convective outflow region topping the developing convective clouds. Below, detrainment of cloudy air into the shells, although weak, generally dominates throughout the convective layer.

Care must be taken when interpreting buoyancy fields shown in Figure 9 because (a) buoyancy in anelastic models is computed with respect to an arbitrarily defined and homogeneous reference environment, and (b) the dynamics of buoyant flows is complicated by the response of the non-hydrostatic pressure field to buoyancy perturbations. To alleviate the problem, an effective buoyancy b_{eff} can be defined following, for example, Davies-Jones (2003):

$$\nabla^2 b_{\text{eff}} = \nabla_H^2 b, \quad (1)$$

where ∇_H represents the horizontal divergence operator. Figure 10 displays composites of b_{eff} for shallow and deep clouds in normalised vertical coordinates. Although b_{eff} shows patterns similar to the traditional buoyancy b , its magnitude is generally reduced. Inside cloud shells,

b_{eff} is again weakly negative, but the inner shell, now defined based on b_{eff} , appears to be even narrower. The most notable feature visible on Figure 10 is perhaps that b_{eff} does not have an obvious in-shell minimum near the top of deep clouds. Note also that the inner-shell region computed based on effective buoyancy now appears to be slightly broader around deeper clouds. Overall, the conclusions drawn previously regarding the role of buoyancy on in-shell subsidence are not strongly affected by the way it is defined.

4.2 | Vertical momentum budget

Vertical momentum budget terms are now composited using the same method as the one described previously, and are plotted on Figure 11 as a function of normalised height in clouds. The vertical momentum equation written in conservative form reads:

$$\underbrace{\frac{\partial \rho_0 w}{\partial t}}_{TOT} = \underbrace{-\frac{\partial \rho_0 u w}{\partial x} - \frac{\partial \rho_0 v w}{\partial y} - \frac{\partial \rho_0 w w}{\partial z}}_{ADV} - \underbrace{\frac{\partial p'}{\partial z}}_{PRES} + \underbrace{+\rho_0 b}_{BUOY} + \tau_w, \quad (2)$$

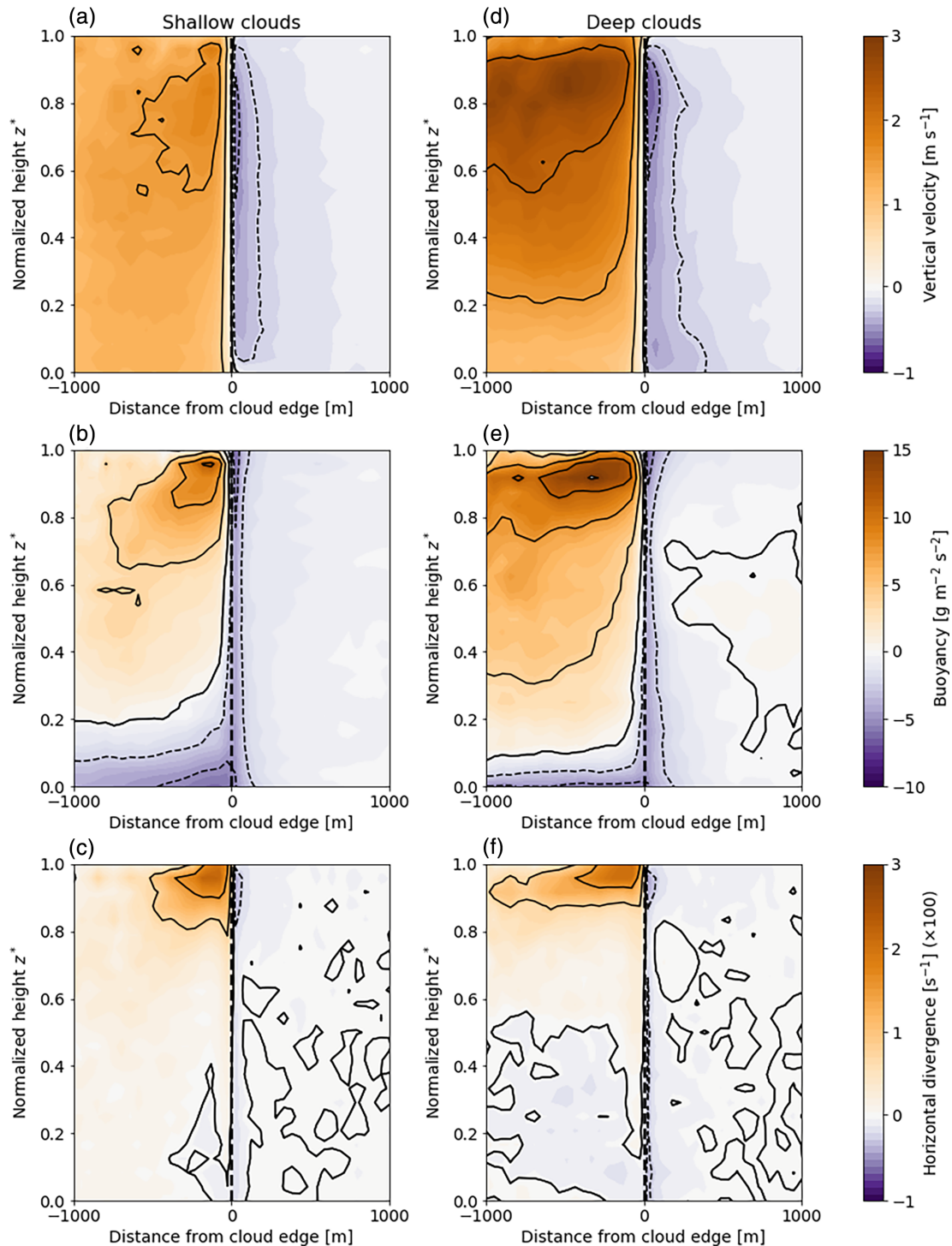


FIGURE 9 (a–c) Shallow and (d–f) deep cloud composites including their near environment, plotted with respect to normalized height in clouds z^* . (a, d) show vertical velocity, (b, e) buoyancy, and (c, f) horizontal wind divergence. The bold vertical dashed lines denote the location of cloud edges; cloud cores are shown on the left of these lines, and the environment is shown on the right. The shells extend from cloud edges into the environment, in the region associated with negative vertical velocities. Contours depicted as thin solid (positive) and dashed (negative) lines were drawn at $[-0.75; -0.5; -0.25; 0; 0.75; 1.5; 2.25; 3] \text{ ms}^{-1}$ in panels (a, d), $[-7.5; -5; -2.5; 0; 3.75; 7.5; 11.25; 15] \text{ g m}^{-2} \text{ s}^{-2}$ in panels (b, e), $[-0.5; -0.25; 0; 0.75; 1.5] \text{ s}^{-1}$ in panels (c, f).

where TOT is the total vertical momentum tendency, ADV represents the contribution from both horizontal and vertical advection, $PRES$ is the vertical pressure gradient

(p' being the perturbation pressure) and $BUOY$ is the buoyancy contribution. Note that b was already plotted on Figure 9 using a different colour scale. Turbulent mixing,

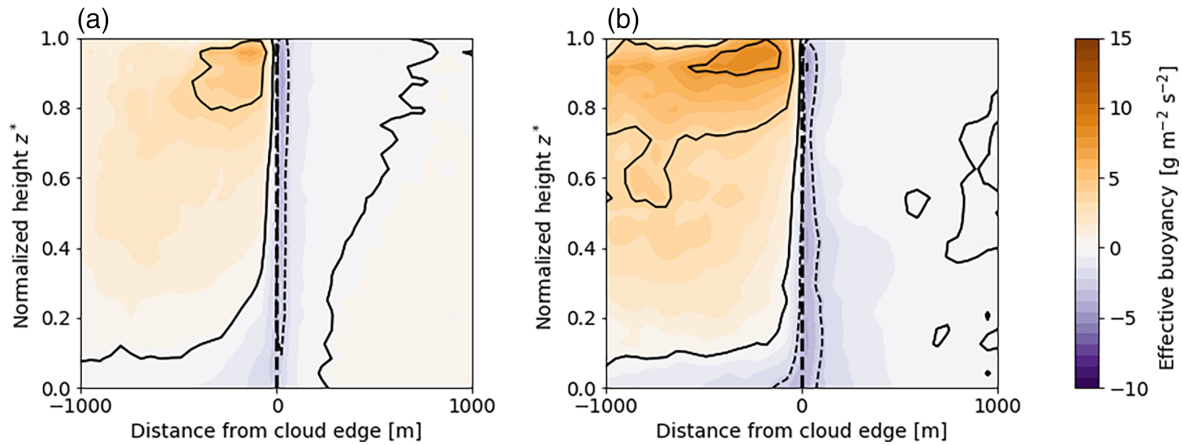


FIGURE 10 (a) Shallow and (b) deep effective buoyancy composites, plotted with respect to normalised height in clouds. Contours depicted as thin solid (positive) and dashed (negative) lines were drawn at $[-5; -2.5; 0; 3.75; 7.5]$ $\text{g m}^{-2} \text{s}^{-2}$.

τ_w , is generally small compared to the other terms and is therefore omitted.

Deep clouds obviously develop in a different environment compared to shallower clouds since they reach higher altitudes. In addition, they were shown to be generally associated with stronger and more buoyant updraught cores. Despite these major differences, the various budget composites displayed on Figure 11 for both shallow and deep clouds are remarkably similar in both pattern and magnitude. All clouds are characterised by strong positive advection at their tops (Figure 11a, e). This strong contribution is to a large extent compensated by a negative pressure gradient (Figure 11c, g). Below, *ADV* remains mostly negative throughout the whole depth of the clouds, except along the edges. Although not shown, *ADV* is to a large extent dominated by its vertical contribution. Near the cloud-top region, both *BUOY* and *PRES* are negative and of similar magnitude within the subsiding shells surrounding all cloud types. Below, pressure gradients inside the shells tend to compensate buoyancy reversal.

In the cloud top region (above $z^* \approx 0.9$), both *BUOY* and *PRES* are negative and of similar magnitude within the subsiding shells surrounding both cloud types. The total vertical momentum budget is here negative and dominated by their combined contributions. Below (especially below $z^* \approx 0.5$), *TOT* remains mostly negative thanks to the dominant contribution from buoyancy, and despite the positive pressure gradients. In-shell *ADV* is generally found to remain weak throughout the convective layer, except near cloud top where detrainment dominates. Overall, *TOT* remains weak within the shells, below the convective outflow region, indicating that subsidence at these levels is only barely sustained.

To further illustrate the role of the various momentum budget terms on in-shell velocity minima w_{\min} , Figure 12 shows density plots of *PRES*, *BUOY* and *ADV* values

estimated at the exact location where w_{\min} is reached within individual shells. While correlations are overall poor, the positive trend observed between *PRES* and w_{\min} indicates that stronger pressure gradients generally result in lower downdraught velocities. As mentioned above, this trend is at least in part compensated by advection. In contrast, no particular trend is found between *BUOY* and w_{\min} , in particular when in-shell subsidence is the strongest. Furthermore, buoyancy generally shows much less variability than either *PRES* or *ADV*. These results are consistent with the fact that stronger buoyancy reversal generally occurs just above the in-shell vertical velocity minimum (e.g., Figure 9).

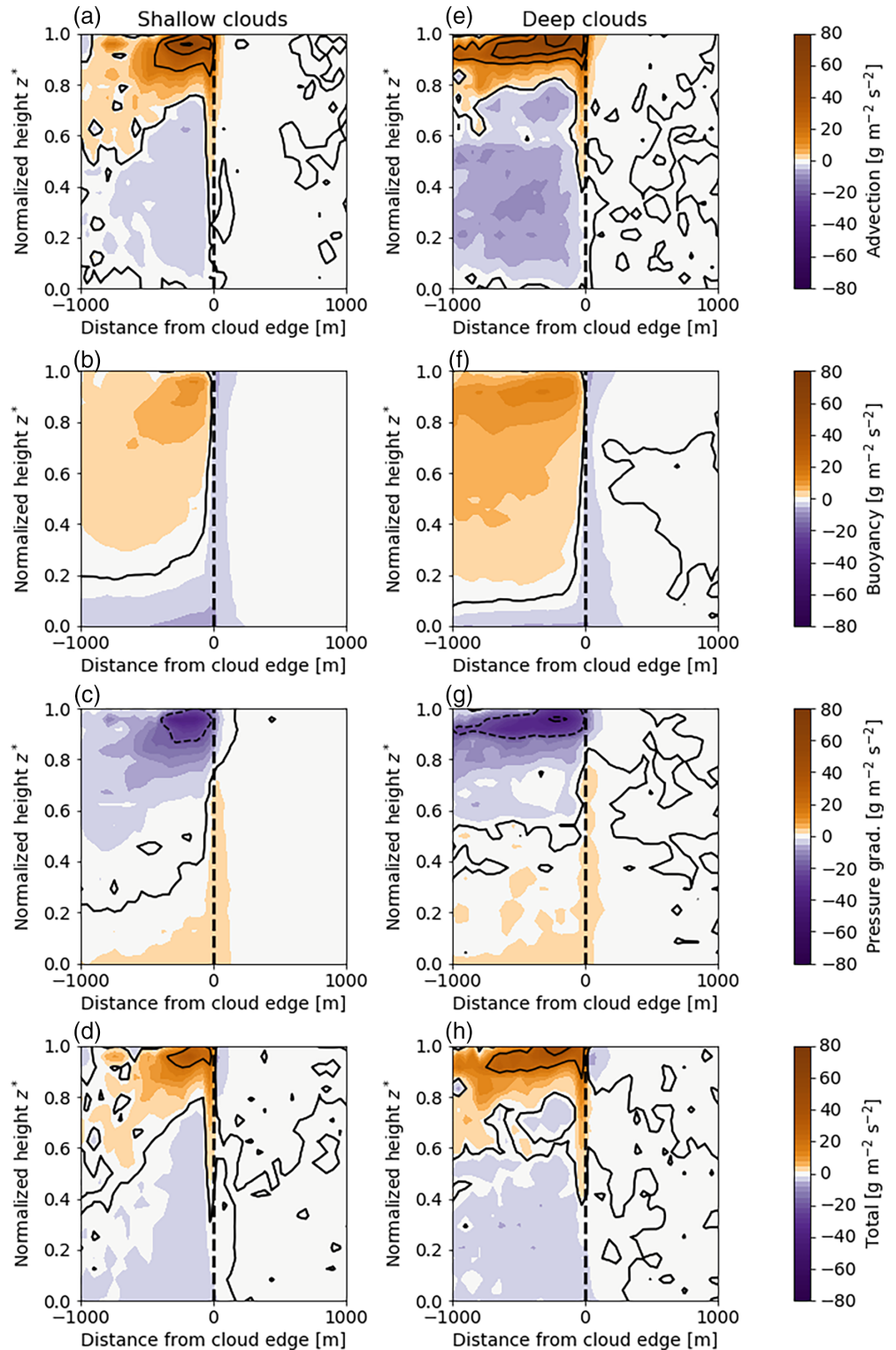
4.3 | Virtual potential temperature budget

Figure 13 displays virtual potential temperature budget terms composited as previously described, as a function of normalized height in clouds z^* . In the absence of radiation and any other external sources and sinks, a virtual potential temperature equation in conservative form can be written:

$$\underbrace{\frac{\partial \rho_0 \theta_v}{\partial t}}_{TOT} = - \underbrace{\frac{\partial \rho_0 u \theta_v}{\partial x} - \frac{\partial \rho_0 v \theta_v}{\partial y} - \frac{\partial \rho_0 w \theta_v}{\partial z}}_{ADV} + \underbrace{+Q}_{PHA} + \tau_{\theta_v}. \quad (3)$$

TOT represents the total virtual potential temperature tendency, *ADV* is the contribution from advection, and *PHA* includes the effects of phase changes only. Again, τ_{θ_v} was found to be generally an order of magnitude smaller than the other terms and is therefore not shown. The virtual potential temperature budget is obviously related to the buoyancy budget, minus a stratification

FIGURE 11 (a–c) Shallow and (d–f) deep cloud composites of the vertical momentum budget terms, plotted with respect to normalised height in clouds z^* . (a, e) advection contribution (*ADV*), (b, f) buoyancy (*BUO*), and (c, g) pressure gradient contribution (*PRES*). (d, h) show the total budget (*TOT*). Contours depicted as thin solid (positive) and dashed (negative) lines were drawn at $[-40; -20; 0; 20; 40; 60] \text{ gm}^{-2}\text{s}^{-2}$.



term of the form $-wN_0^2\theta_v/\theta_{v0}$, with $N_0^2 = g/\theta_{v0} \partial\theta_{v0}/\partial z$ being the Brünt–Väisälä frequency calculated based on the reference atmospheric state. With $N_0^2 > 0 \text{ s}^{-2}$ in the free troposphere and $w < 0 \text{ m}\cdot\text{s}^{-1}$ inside the subsiding shells, this term contributes positively to the buoyancy budget and acts as an additional source of positive buoyancy

within the shells. For comparison with Figure 13, taking $w = -1 \text{ m}\cdot\text{s}^{-1}$ stratification contributes $\sim 4 \times 10^{-3} \text{ K}\cdot\text{s}^{-1}$ in temperature units to the buoyancy budget and is therefore much smaller than the other budget terms displayed.

Again, the θ_v budget composites computed for both shallow and deep clouds are strikingly similar. Examining

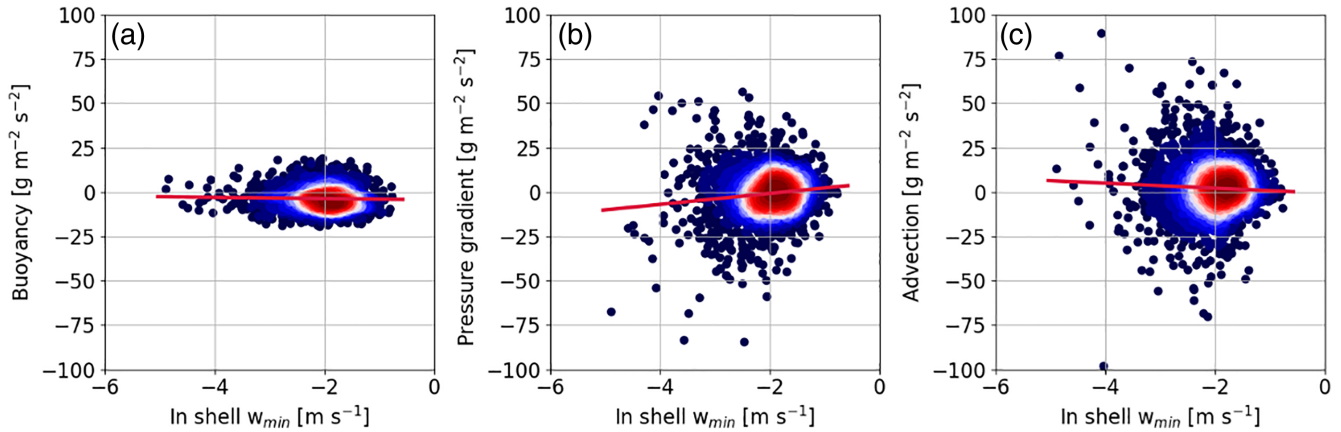


FIGURE 12 Density plots of (a) buoyancy, (b) pressure gradient and (c) vertical momentum advection as functions of minimum shell vertical velocity. The solid red lines were obtained by linear regression

the different contributions to the total budget, in-cloud buoyancy production is, as expected, dominated by *PHA* thanks to strong latent heat release from condensation. *ADV* contributes negatively throughout most of the cloud layer, except near the convective outflow region where it clearly dominates buoyancy production. *ADV* is here again clearly dominated by its vertical contribution throughout the cloud layer, except within a very shallow layer situated at cloud top (not shown). Overall, *TOT* remains mostly negative inside cloud cores, except in a shallow region near cloud top.

As expected, $PHA < 0$ inside the shells independently of cloud type and altitude, indicating that evaporative cooling is the main source of buoyancy reversal in the near-cloud environment. *PHA* then increases progressively when moving away from the cloud edge, and becomes ~ 0 approximately 100 and 200 m into the environment for shallow and deep clouds respectively (this corresponds approximately to the mean inner shell width estimated in Section 3.1). In the near-cloud environment at cloud top, *ADV* is weaker than *PHA* but also contributes to buoyancy reversal. Below, *ADV* remains weakly positive along all clouds.

In the near-cloud environment, *TOT* is mostly negative and reaches a minimum in the shallow detrainment layer at cloud top. Negative *TOT* values within cloud shells extend approximately down to $z^* = 0.3$. Below, *TOT* becomes weakly positive as the *ADV* and *PHA* contributions balance. Since *ADV* mostly reflects the contribution from vertical advection, $ADV > 0$ within the near-cloud environment reflects the downward transport of less dense environmental air from aloft through the subsiding shell. Downward transport within the shells can therefore affect the local thermodynamic balance to the extent that the corresponding warming may offset evaporative cooling to yield positive net buoyancy tendencies.

4.4 | Comparison to previous studies

Some of the conclusions drawn previously regarding the mechanisms driving in-shell subsidence and buoyancy reversal are here compared to previous works.

While it was shown that buoyancy reversal acts as a constant source of subsidence throughout the cloud layer, mechanical forcing (pressure gradients) was found to be at least equally important in generating subsidence in the convective outflow region near cloud top. Using a similar vertical momentum budget analysis, Heus and Jonker (2008) concluded that buoyancy reversal was clearly the dominant source of in-shell subsidence. Advection and pressure gradients, both contributing positively, compensated only partly for the negative buoyancy anomalies. These results agree well with Figure 11 in a region located below $z^* < 0.8$. However, since they were obtained from horizontal cuts through shallow cumuli at a single altitude, the shell's dynamics in the cloud top region could not be analysed with the same level of detail as here. A more comprehensive view of the dynamics of cloudy thermals and their subsiding shells can be found in Romps and Charn (2015). Although investigating the shell's dynamics was not their primary focus, their results also tend to indicate that lateral subsidence around cloudy thermals happens where pressure gradients contribute at least as much as buoyancy.

It should be noted that elementary fluid mechanics predicts that a dry, buoyant mass of fluid initially at rest will develop into a vortex ring composed of an accelerating buoyant bubble surrounded by a subsiding shell (Scorer and Ludlam, 1953; Malkus and Scorer, 1955; Woodward, 1959). This latter arises mostly from baroclinic vorticity production, and is independent of evaporation and microphysics. Although care should always be taken when comparing such idealized configurations with real-life clouds,

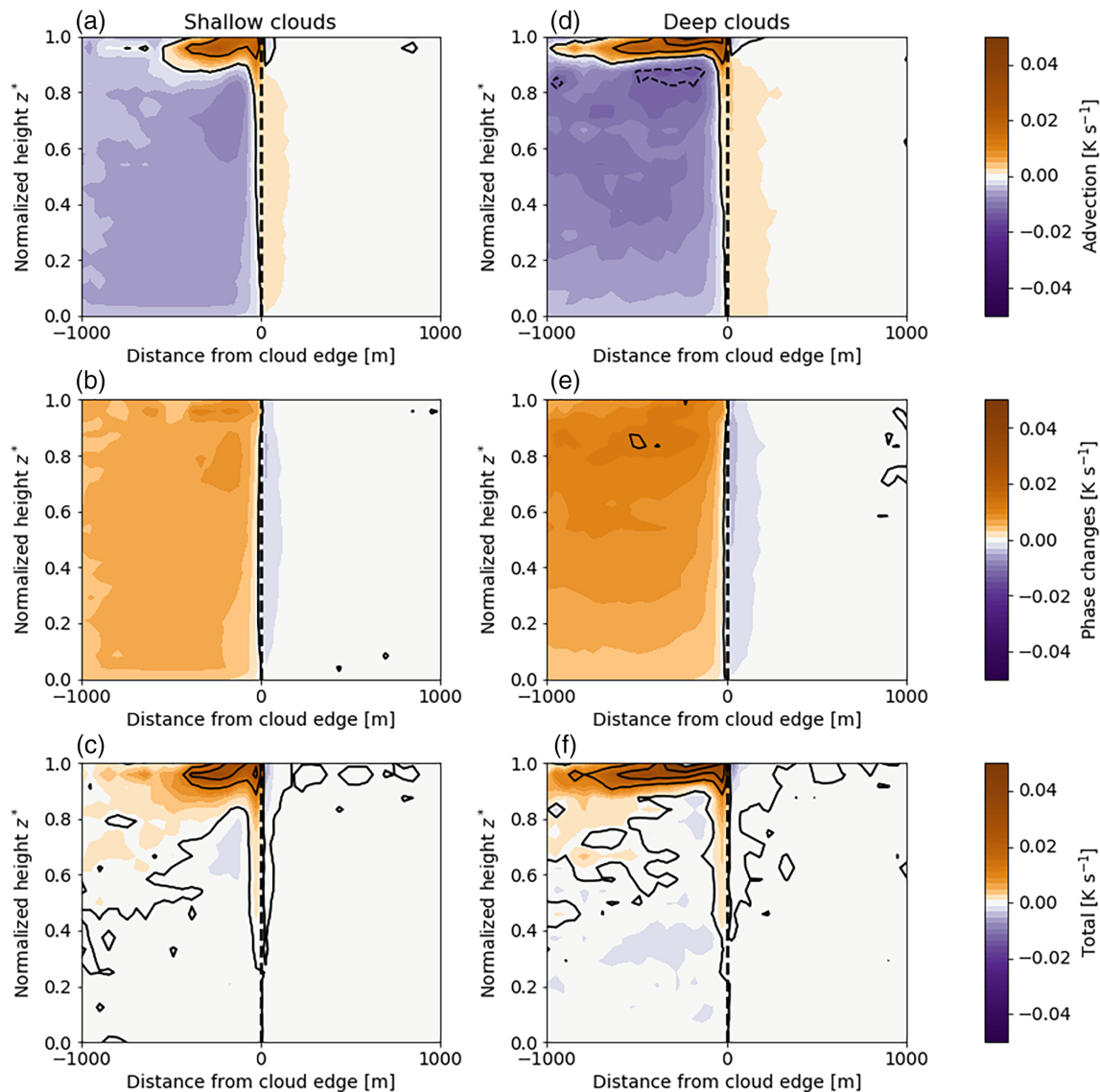


FIGURE 13 As Figure 11, but for the virtual potential temperature budget: (a, d) advection (*ADV*), (b, e) evaporation/condensation (*PHA*), and (c, f) total budget (*TOT*). Contours depicted as thin solid (positive) and dashed (negative) lines were drawn at $[-0.0125; 0; 0.0125; 0.025; 0.0375; 0.05] \text{ K s}^{-1}$.

a similar structure was also found to characterize more realistic cloudy thermals in Sherwood *et al.* (2013) and Romps and Charn (2015), in line with the vertical velocity composites shown in Figure 9. Of course, and despite the fact that pressure gradients contribute significantly to the generation of subsidence near cloud top, the overall role of buoyancy reversal in forcing and maintaining a consistent subsiding shell throughout the convective cloud layer should not be minimised.

The virtual potential temperature budget composites displayed in Figure 13 revealed that evaporative cooling is generally the dominant source of negative buoyancy anomalies throughout the cloud depth. That evaporative cooling yields buoyancy reversal, and is thus indirectly responsible for in-shell subsidence, agrees with most

recent numerical (Heus and Jonker, 2008; Glenn and Krueger, 2014) and observational (Wang *et al.*, 2009; Katzwinkel *et al.*, 2014; Mallaun *et al.*, 2019) studies of cumulus cloud shells. In the present study, detrainment was also shown to contribute to negative buoyancy anomalies in the convective outflow region. This contribution was however found to remain weak and to be restricted to a relatively small region of the near-cloud environment. Therefore it appears difficult to conclude following Park *et al.* (2017) that evaporative cooling is generally of secondary importance in generating buoyancy reversal. Finally, downward transport through the subsiding shells was found to be able to offset evaporative cooling in the lower part of the clouds to yield positive net buoyancy tendencies in the near-cloud environment. To the best of

our knowledge, this is the first time that such a strong impact of in-shell transport on the shell's dynamics is demonstrated.

5 | CONCLUSION

In an attempt to better characterise the vertical structure and the dynamics of subsiding shells surrounding cumulus clouds, a high-resolution (25 m in the horizontal) cloud-resolving model simulation was performed and analysed, with a particular emphasis on the cloud's near environment. The numerical set-up is based on a well-documented intercomparison study that focused on the diurnal transition between shallow and deep tropical convection in a continental environment. As such, it was also possible to identify differences in the structure and driving mechanisms of shells developing around shallow and deeper clouds.

Below about 2,000 m, all clouds, shallow and deep, are characterized by shells maintaining similar, altitude-independent strengths ($\sim -1 \text{ m}\cdot\text{s}^{-1}$) and widths ($\sim 400 \text{ m}$). Above, the shells surrounding the deepest clouds tend to become stronger and wider with altitude, with both quantities reaching extrema slightly below cloud top. Despite many shell points being positively buoyant at all altitudes, all clouds are on average surrounded by a very narrow ($\sim 150 \text{ m}$ wide) inner shell defined as the negatively buoyant part of the subsiding shell. The inner shell is generally found to occupy on average a third to a half of the whole subsiding shell.

As expected, cloud shells were found to be moister and colder than the environment at a given altitude. A clear signature of lateral mixing (detrainment) between the clouds and their environment was found inside the shells with in-shell *MSE* lying on average between in-cloud and environmental values at any given altitude. Although this could not be verified, a mixing diagram analysis also revealed that downward air transport inside the shells may also contribute to local in-shell thermodynamics.

Cloud composites were then constructed from two-dimensional slices extracted from the full three-dimensional simulation. The compositing procedure allows us to directly analyse the horizontal and vertical structure of simulated cloud shells. Applying the compositing procedure to vertical momentum and virtual potential temperature budget terms, the detailed dynamics of both cloud cores and, more importantly, subsiding shells could be investigated. Overall, the main results of this analysis can be summarised as follows:

1. The vertical structure of subsiding shells follows closely that of the corresponding cloud cores, with shallow, plume-like clouds characterised by a relatively

homogeneous shell, while deeper, bubble-like clouds clearly exhibit a velocity minimum near their top.

2. In-shell buoyancy is on average negative throughout the cloud layer and consistently contributes to maintaining in-shell subsidence.
3. In the convective outflow region, mechanical forcing from negative pressure gradients seems to be at least as important as buoyancy reversal for generating in-shell subsidence.
4. Below, positive contributions from horizontal advection (detrainment) and pressure gradients may, exceed buoyancy reversal. In-shell subsidence is however overall very weakly forced below the cloud-top region.
5. Evaporative cooling clearly supports buoyancy reversal along cloud edges at all altitudes. However, the downward transport of warmer air from aloft through the subsiding shells can be significant enough near cloud base to actually counterbalance the effects of evaporative cooling.

Combining these results, we can now draw a simple picture that summarises the dynamics of subsiding cloud shells. The combined effects of buoyancy reversal and negative pressure gradients generate and force subsidence near cloud top. The strong mechanical forcing observed there is a result of cloud-top vortex dynamics, which indicates that evaporative cooling and buoyancy reversal are not the sole processes contributing to the formation of a subsiding shell in this region. Along cloud edges, below the outflow region and down to cloud base, pressure gradients (for momentum) and downward transport through the subsiding shells (for buoyancy) both act against the contribution from evaporative cooling that maintains a negatively buoyant shell. If we except the cloud-top region where subsidence is continuously forced, in-shell subsidence is therefore barely sustained by a delicate balance of various processes mitigating the dominant impact of evaporative cooling.

Although this was out of the scope of the present study, the results presented here can guide the development of more accurate convection parametrizations that would explicitly include the impact of subsiding shells on the evolution of cumulus clouds. For instance, it was found that shells surrounding plume-like shallow clouds generally conserve relatively constant properties (width and strength) throughout their depth. As such, it might be possible to complement existing entraining plume models with a buffer region (representing the shell) of constant width and velocity between the environment and the cloud. Another possible way of improvement could be through the modification of the buoyancy sorting concept frequently used to model entrainment/detrainment in convection parametrizations. While buoyancy sorting

assumes that evaporative cooling alone determines the fate of cloudy air parcels mixed with the environment, the present results reveal that dynamics generally cannot be ignored.

Of course, it must be recalled here that these results are limited to a single case-study and may depend strongly on environmental conditions. In particular, we can expect environmental moisture to play an important role in the processes highlighted in this study. A drier atmosphere may promote evaporation along cloud edges and possibly lead to a more dominant impact of buoyancy reversal on shell dynamics. In contrast, a moister atmosphere may limit buoyancy reversal along cloud edges leading to faster recovery of in-shell subsidence, and perhaps even to the disappearance of the shell structures. Although other authors have formulated similar conclusions based on different simulated cases, it will be interesting to further test these hypotheses under a wider range of conditions. Besides, all clouds analysed in this study were sampled without regard to their development stage. Since actively growing clouds are dynamically different from decaying clouds, the results presented may be sensitive to the cloud's life cycles. This stresses the need for a more careful investigation of the transient development of subsiding shells as their parent clouds grow and decay.

ACKNOWLEDGEMENTS

The author would like to thank the Leibniz-RechenZentrum (LRZ, Garching) for providing the high-performance computing facilities on which the simulations presented in this manuscript were performed. Open access funding enabled and organized by Projekt DEAL.

ORCID

Julien Savre  <https://orcid.org/0000-0003-3104-6987>

REFERENCES

- Abma, D., Heus, T. and Mellado, J.P. (2013) Direct numerical simulation of evaporative cooling at the lateral boundary of shallow cumulus clouds. *Journal of the Atmospheric Sciences*, 70, 2088–2102.
- Blyth, A.M., Cooper, W.A. and Jensen, J.B. (1988) A study of the source of entrained air in Montana cumuli. *Journal of the Atmospheric Sciences*, 45, 3944–3964.
- Blyth, A.M., Lasher-Trapp, S.G. and Cooper, W.A. (2005) A study of thermals in cumulus clouds. *Quarterly Journal of the Royal Meteorological Society*, 131, 1171–1190.
- Böing, S.J., Jonker, H.J.J., Siebesma, A.P. and Grabowski, W.W. (2012) Influence of the subcloud layer on the development of a deep convective ensemble. *Journal of the Atmospheric Sciences*, 69, 2682–2698.
- Craig, G.C. and Dörnbrack, A. (2008) Entrainment in cumulus clouds: what resolution is cloud-resolving?. *Journal of the Atmospheric Sciences*, 65, 3978–3988.
- Damiani, R., Vali, G. and Haimov, S. (2006) The structure of thermals in cumulus from airborne dual-Doppler radar observations. *Journal of the Atmospheric Sciences*, 63, 1432–1450.
- Davies-Jones, R. (2003) An expression for effective buoyancy in surroundings with horizontal density gradients. *Journal of the Atmospheric Sciences*, 60, 2922–2925.
- Dawe, J.T. and Austin, P.H. (2011) The influence of the cloud shell on tracer budget measurements of LES cloud entrainment. *Journal of the Atmospheric Sciences*, 68, 2909–2920.
- de Rooy, W.C., Bechtold, P., Fröhlich, K., Hohenegger, C., Jonker, H., Mironov, D., Siebesma, P.A., Teixeira, J. and Yano, J.-I. (2012) Entrainment and detrainment in cumulus convection: an overview. *Quarterly Journal of the Royal Meteorological Society*, 139, 1–19.
- Glenn, I.B. and Krueger, S.K. (2014) Downdrafts in the near-cloud environment of deep convective updrafts. *Journal of Advances in Modeling Earth System*, 6, 1–8.
- Grabowski, W.W. (1998) Toward cloud resolving modeling of large-scale tropical circulations: a simple cloud microphysics parameterization. *Journal of the Atmospheric Sciences*, 55, 3283–3298.
- Grabowski, W.W., Bechtold, P., Cheng, A., Forbes, R., Halliwell, C., Khairoutdinov, M., Lang, S., Nasuno, T., Petch, J., Tao, W.-K., Wong, R., Wu, X. and Xu, K.-M. (2006) Daytime convective development over land: a model intercomparison based on LBA observations. *Quarterly Journal of the Royal Meteorological Society*, 132, 317–344.
- Hannah, W.M. (2017) Entrainment and dilution in tropical deep convection. *Journal of the Atmospheric Sciences*, 74, 3725–3747.
- Heus, T. and Jonker, H.J.J. (2008) Subsiding shells around shallow cumulus clouds. *Journal of the Atmospheric Sciences*, 65, 1003–1018.
- Heus, T., Pols, J., Freek, C., Jonker, H.J.J., den Akker, A.V., Harry, E. and Lenschow, D.H. (2009) Observational validation of the compensating mass flux through the shell around cumulus clouds. *Quarterly Journal of the Royal Meteorological Society*, 135, 101–112.
- Jonas, P.R. (1990) Observations of cumulus cloud entrainment. *Atmospheric Research*, 25, 105–127.
- Jonker, H.J.J., Heus, T. and Sullivan, P.P. (2008) A refined view of vertical mass transport by cumulus convection. *Geophysical Research Letters*, 35, L07810
- Katzwinkel, J., Siebert, H., Heus, T. and Shaw, R.A. (2014) Measurements of turbulent mixing and subsiding shells in trade wind cumuli. *Journal of the Atmospheric Sciences*, 71, 2810–2822.
- Lipps, F.B. and Hemler, R.S. (1982) A scale analysis of deep moist convection and some related numerical calculations. *Journal of the Atmospheric Sciences*, 39, 2192–2210.
- Lu, C., Liu, Y., Zhang, G.J., Wu, X., Endo, S., Cao, L., Li, Y. and Guo, X. (2016) Improving parameterization of entrainment rate for shallow convection with aircraft measurements and large-eddy simulation. *Journal of the Atmospheric Sciences*, 73, 761–773.
- Malkus, J. and Scorer, R.S. (1955) The erosion of cumulus towers. *Journal of Meteorology*, 12, 43–57.
- Mallaun, C., Giez, A., Mayr, G.J. and Rotach, M.W. (2019) Subsiding shells and the distribution of up- and downdrafts in warm cumulus clouds over land. *Atmospheric Chemistry and Physics*, 19, 9769–9786.

- Moeng, C.-H. (1984) A large-eddy-simulation model for the study of planetary boundary-layer turbulence. *Journal of the Atmospheric Sciences*, 41, 2052–2062.
- Nair, V., Heus, T. and van Reeuwijk, M. (2019) Dynamics of subsiding shells in actively growing clouds with vertical updrafts. *Journal of the Atmospheric Sciences*
- Park, S.-B., Gentine, P., Schneider, K. and Farge, M. (2016) Coherent structures in the boundary and cloud layers: role of updrafts, subsiding shells, and environmental subsidence. *Journal of the Atmospheric Sciences*, 73, 1789–1814.
- Park, S.-B., Heus, T. and Gentine, P. (2017) Role of convective mixing and evaporative cooling in shallow convection. *Journal of Geophysical Research: Atmospheres*, 122, 5351–5363.
- Rodts, S.M.A., Duynkerke, P.G. and Jonker, H.J.J. (2003) Size distributions and dynamical properties of shallow cumulus clouds from aircraft observations and satellite data. *Journal of the Atmospheric Sciences*, 60, 1895–1912.
- Romps, D.M. (2010) A direct measure of entrainment. *Journal of the Atmospheric Sciences*, 67, 1908–1927.
- Romps, D.M. and Charn, A.B. (2015) Sticky thermals: evidence for a dominant balance between buoyancy and drag in cloud updrafts. *Journal of the Atmospheric Sciences*, 72, 2890–2901.
- Romps, D.M. and Kuang, Z. (2010) Do undiluted convective plumes exist in the upper tropical troposphere?. *Journal of the Atmospheric Sciences*, 67, 468–484.
- Rougier, J., Sexton, D.M.H., Murphy, J.M. and Stainforth, D. (2009) Analyzing the climate sensitivity of the HADSM3 climate model using ensembles from different but related experiments. *Journal of Climate*, 22, 3540–3557.
- Savre, J., Ekman, A.M.L. and Svensson, G. (2014) Technical note: introduction to MIMICA, a large-eddy simulation solver for cloudy planetary boundary layers. *Journal of Advances in Modeling Earth System*, 6, 630–649.
- Schmeissner, T., Shaw, R.A., Ditas, J., Stratmann, F., Wendisch, M. and Seibert, H. (2015) Turbulent mixing in shallow trade wind cumuli: dependence on cloud life cycle. *Journal of the Atmospheric Sciences*, 72, 1447–1465.
- Scorer, R.S. and Ludlam, F.H. (1953) Bubble theory of penetrative convection. *Quarterly Journal of the Royal Meteorological Society*, 79, 94–103.
- Sherwood, S.C., Hernández-Deckers, D., Colin, M. and Robinson, F. (2013) Slippery thermals and the cumulus entrainment paradox. *Journal of the Atmospheric Sciences*, 70, 2426–2442.
- Soares, P.M.M., Miranda, P.M.A., Siebesma, A.P. and Teixeira, J. (2004) An eddy diffusivity/mass flux parametrization for dry and shallow cumulus convection. *Quarterly Journal of the Royal Meteorological Society*, 130, 3365–3384.
- Tiedtke, M. (1989) A comprehensive mass flux scheme for cumulus parameterization in large-scale models. *Monthly Weather Review*, 117, 1779–1800.
- Wang, Y. and Geerts, B. (2010) Humidity variations across the edge of trade wind cumuli: observations and dynamical implications. *Atmospheric Research*, 97, 144–1156.
- Wang, Y., Geerts, B. and French, J. (2009) Dynamics of the cumulus cloud margin: an observational study. *Journal of the Atmospheric Sciences*, 66, 3660–3677.
- Woodward, B. (1959) The motion in and around isolated thermals. *Quarterly Journal of the Royal Meteorological Society*, 85, 144–151.
- Wu, C.-M., Stevens, B. and Arakawa, A. (2009) What controls the transition from shallow to deep convection?. *Journal of the Atmospheric Sciences*, 66, 1793–1806.
- Zhang, G.J., Wu, X., Zeng, X. and Mitovski, T. (2016) Estimation of convective entrainment properties from a cloud-resolving model simulation during TWP-ICE. *Climate Dynamic*, 47, 2177–2192.

How to cite this article: Savre J. Formation and maintenance of subsiding shells around non-precipitating and precipitating cumulus clouds. *QJR Meteorol Soc.* 2020;1–18. <https://doi.org/10.1002/qj.3942>